Computers and Fluids 269 (2024) 106136

Contents lists available at ScienceDirect

Computers and Fluids

journal homepage: www.elsevier.com/locate/compfluid

A stable scheme of the Curvilinear Shallow Water Equations with no-penetration and far-field boundary conditions

Reindorf Nartey Borkor [a,b,*], Magnus Svärd [c], Peter Amoako-Yirenkyi [a,b]

[a] Center for Scientific and Technical Computing, National Institute for Mathematical Sciences (NIMS), Ghana
[b] Department of Mathematics, Kwame Nkrumah University of Science and Technology (KNUST), Ghana
[c] Department of Mathematics, University of Bergen, Bergen, Norway

ARTICLE INFO

MSC:
65M06
65M12
35L65
35F61

Keywords:
Hydrodynamic
Summation-by-parts (SBP)
Simultaneous Approximation Terms (SAT)
High-order finite-difference methods
Stability
Well-posedness

ABSTRACT

This paper presents a stable and highly accurate numerical tool for computing river flows in urban areas, which is a first step towards a numerical tool for flood predictions. We start with the (linearized) well-posedness analysis by Ghader and Nordström (2014), where far-field boundary conditions were proposed and extend their analysis to include wall boundaries. Specifically, we employed high-order Summation-by-parts (SBP) finite-difference operators to construct a scheme for the Shallow Water Equations. We also developed a stable SBP scheme with Simultaneous Approximation Terms that impose far-field and wall boundaries. Finally, we extended the schemes and their stability proofs to non-Cartesian domains. To demonstrate the strength of the schemes, we performed computations for problems with exact solutions to obtain second, third, and fourth (2, 3, 4) convergence rates. Finally, we applied the $4th$-order scheme to steady river channels, the canal (or flood-control channel simulations), and dam-break problems. The results show that the imposition of the boundary conditions is stable, and the far-field boundaries cause no visible reflections at the boundaries.

1. Introduction

Over the years, tragic events due to flooding have been recorded annually in many cities, usually causing the loss of both lives and properties. For example, in June 2015, over one hundred and fifty (150) people died as a result of mainly flooding in Ghana, see the report [1]. Apart from natural factors that cause flooding, such as intense rainfall stimulating internal erosion and surface run-offs, other contributing factors, such as urbanization, land use, and poor channels, have aggravated the impact of floods in cities [2–4]. The problem of flooding persists, and it is generally encountered in many parts of the world today. Due to this, an improvement in the simulation tools that accurately predict flood events is needed.

Flood propagation can, in principle, be modelled by the Navier–Stokes Equations (NSE), but these equations are too computationally expensive to solve [5,6]. Instead, we consider the Shallow Water equations (SWE) obtained by depth-integrating the NSE. The SWE describe the evolution of a shallow layer of fluid and are useful in the simulation of open-channel flows and large-scale hydraulics, to mention a few examples. (See [5–10] for more details). Mathematically, the SWE are a system of non-linear conservation laws that generally requires computational methods to approximate solutions. Solutions can contain shocks, but herein we focus on smooth solutions. For smooth solutions, high-order accurate numerical schemes are typically more efficient [11–17].

The primary focus of this paper is to develop a highly accurate numerical tool for computing the flow of rivers. In the longer term, this tool can be then extended to handle flood waves and flooding. To this end, we begin by deriving well-posed boundary conditions of the Shallow Water Equations and stable high-order schemes for the resulting initial–boundary value problems. To reduce notation, and since the bottom topography does not influence the treatment of the boundaries, we consider a flat bottom. The set of well-posed far-field boundary conditions for the Shallow Water Equations have been derived by [18], and [19] for the one-dimensional (1-D) and 2-D cases, respectively. In [19], they derived generic open boundary conditions (B.C.) for a general domain but did not consider wall boundary conditions or numerical methods for implementing the boundary conditions. Lundgren and Mattsson [14] used the characteristic boundary conditions in their work, albeit in a very different way from what we shall consider in this study. However, their formulation was done in a component-wise fashion. Although they took into account the Cartesian multi-block boundaries, they did not consider the wall B.C. Additionally, Nordström and Winters looked at a comparison study of linear and nonlinear analysis and how it affected the ability to predict the characteristics

---

* Corresponding author at: Department of Mathematics, Kwame Nkrumah University of Science and Technology (KNUST), Ghana.
E-mail addresses: reinbork@knust.edu.gh (R.N. Borkor), Magnus.Svard@uib.no (M. Svärd), amoakoyirenkyi@knust.edu.gh (P. Amoako-Yirenkyi).

https://doi.org/10.1016/j.compfluid.2023.106136
Received 11 June 2023; Received in revised form 28 October 2023; Accepted 23 November 2023

of the B.C. [20]. But in their case, they also did not consider wall and multi-block boundaries.

To advance the research of the studies as mentioned earlier, we rederive the set of far-field boundary conditions in [19] and take into account the following: First, we show that the Summation-by-Parts Simultaneous Approximation Term (SBP-SAT) scheme, which is used to implement the B.C., is stable. We further show that the boundary conditions for no-penetration walls are well-posed and derive a stable SBP-SAT scheme. As an extension to the previous studies, we also consider, in this work, the curvilinear generalization to a general domain; we generalize the schemes and the stability proofs to a curvilinear frame for the complete initial–boundary value problem since realistic flows are usually not limited to Cartesian domains. We note, however, that we do not consider the capability of the stable schemes for multi-block grids in a curvilinear domain in this work, and we postpone the analysis to later work. We verify the scheme using the method of manufactured solutions (see [21,22]) and then apply it to a set of flood propagation problems.

The paper is outlined as follows: Section 2 introduces the definitions and concepts underpinning the theory of the linear Initial Boundary Value problem (IBVP). The 2-D SWE are presented in Section 3. Section 4 establishes the linear well-posedness analysis with continuous energy estimates of the 2-D SWE, including boundary conditions. Further, in Section 5, we construct high-order SBP-SAT finite-difference schemes that satisfy discrete energy estimates that mimic the corresponding estimates. Also, in Section 6, we propose a general case of the stability proofs by deriving Curvilinear Shallow Water Equations. Finally, Section 7 provides numerical experiments that verify the analysis carried out in Sections 4–6.

2. Concepts and definitions

Let $\Omega = \{(x, y) : 0 \leq x \leq 1, 0 \leq y \leq 1\}$ denote the spatial domain in 2-D and $\partial\Omega$ denote its boundary. Consider the following IBVP:

$$\begin{aligned} u_t + Pu &= F(x, y, t), \quad (x, y) \in \Omega, \quad 0 < t < T, \quad (T \text{ is the final time}), \\ Bu &= g(x, y, t), \quad (x, y) \in \partial\Omega, \quad t \geq 0, \\ u &= f(x, y), \quad (x, y) \in \Omega, \quad t = 0, \end{aligned} \tag{1}$$

where $u(x, y, t)$ represents the solution vector. P and B denote the spatial linear differential and boundary operators, respectively. Furthermore, F is a forcing function. Finally, g and f are smooth boundary and initial data, respectively.

The scalar product and norm are defined as,

$$(w, v)_\Omega = \int_\Omega w^T v\, dx\, dy, \quad \|w(\cdot, t)\|^2_\Omega = (w, w)_\Omega, \tag{2}$$

for real-valued vector functions w and v. We need the Definitions 1–2 below, that are found in [13,23].

Definition 1. The IBVP (1) with $F = g = 0$ is *well posed* if for every $f \in C^\infty$ that vanishes in a neighbourhood of $\partial\Omega$, a unique smooth solution exists that satisfies the estimate

$$\|u(\cdot, t)\|^2_\Omega \leq K^c_1 e^{\alpha_c t} \|f\|^2_\Omega, \quad 0 < t < T,$$

where K^c_1 and α_c are constant values which are also bounded independently of f.

Sometimes, the solution can be bounded with $F \neq 0, g \neq 0$. Then we say that the problem is *strongly well-posed.*

Next, we turn to the discretization of (1). Let $x_i = i\mathsf{h}_1, i = 0, 1, \ldots, M$ and $y_j = j\mathsf{h}_2, j = 0, 1, \ldots, N$ where respectively, $\mathsf{h}_1 = 1/M$ and $\mathsf{h}_2 = 1/N$ are the grid spacings. Now, the following sets of indices are defined for the interior and boundaries: $\mathcal{I}_1 = \{(i, j) : i = 1 \ldots, M - 1, j = 1, \ldots, N - 1\}$, $\mathcal{I}_2 = \{(i, j) : i = 0, M, \forall j\}$, and $\mathcal{I}_3 = \{(i, j) : \forall i; j = 0, N\}$. That is, $\mathcal{I}_1$ holds all interior points whiles $\mathcal{I}_2$ and $\mathcal{I}_3$ hold all boundary points. We introduce the semi-discrete approximation of (1),

$$\begin{aligned} (v_{ij})_t + P_\mathsf{h} v_{ij} &= F_{ij}, \quad (i, j) \in \mathcal{I}_1, \quad t \geq 0, \\ B_\mathsf{h} v_{ij} &= g_{ij}, \quad (i, j) \in \mathcal{I}_2, \mathcal{I}_3, \quad t \geq 0, \\ v_{ij} &= f_{ij}, \quad (i, j) \in \mathcal{I}_1 \cup \mathcal{I}_2 \cup \mathcal{I}_3, \quad t = 0, \end{aligned} \tag{3}$$

where $v_{ij}(t)$ is the approximate solution at grid point (x_i, y_j). We denote the grid function defined on $\mathcal{I}_1 \cup \mathcal{I}_2 \cup \mathcal{I}_3$ as v such that $[v]_{ij} = v_{ij}$. The difference operator P_h approximates P and B_h is a discrete boundary operator approximating B. $F_{ij} = F(x_i, y_j, t), g_{ij} = g(x_i, y_j, t)$ and $f_{ij} = f(x_i, y_j)$ are the known compatible data of (1). (See [13] for an explanation of compatibility.)

The definition of the discrete scalar product and the norm are given as

$$(w, v)_\mathsf{h} = w^T \mathbf{P} v \qquad \|w\|^2_\mathsf{h} = (w, w)_\mathsf{h}, \tag{4}$$

for real grid vector functions w and v. Here, $\mathbf{P}$ is a positive definite symmetric matrix to be defined later. It approximates the integration operation in (2).

Definition 2. Let (3) be a semi-discrete approximation of the well-posed problem (1) with $F = g = 0$. Then the semi-discrete approximation (3) is stable if the solution v satisfies the estimate

$$\|v(t)\|^2_\mathsf{h} \leq K^d_1 e^{\alpha_d t} \|f\|^2_\mathsf{h},$$

where K^d_1 and α_d are constants which are bounded and independent of f.

Analogous to the continuous problem, if the numerical solution can be bounded with $F \neq 0$ and $g \neq 0$, we say that the problem is *strongly stable.*

3. The continuous problem

3.1. Shallow Water Equations

The 2-D nonlinear Shallow Water Equations are

$$\mathcal{W}_t + [\mathcal{F}(\mathcal{W})]_x + [\mathcal{G}(\mathcal{W})]_y = 0, \quad (x, y) \in \Omega, \quad t > 0, \tag{5}$$

where

$$\mathcal{W} = \begin{pmatrix} h \\ hu \\ hv \end{pmatrix}, \quad \mathcal{F}(\mathcal{W}) = \begin{pmatrix} hu \\ hu^2 + \mathsf{g}h^2/2 \\ huv \end{pmatrix}, \quad \mathcal{G}(\mathcal{W}) = \begin{pmatrix} hv \\ huv \\ hv^2 + \mathsf{g}h^2/2 \end{pmatrix}.$$

$\mathcal{W}$ is the vector consisting of the conserved variables. The convective flux-vector functions are $\mathcal{F}(\mathcal{W})$ and $\mathcal{G}(\mathcal{W})$, respectively, in the x- and y-direction. $h(t, x, y)$ is the depth of water (or height) and hu and hv are, the momentum in the x- and y-direction. Furthermore, g is the gravitational constant and $u(t, x, y)$ and $v(t, x, y)$ are the velocity components in x- and y-direction, respectively (see [5]).

The 1-D form of (5) is given as

$$\mathcal{W}_t + [\mathcal{F}(\mathcal{W})]_x = 0, \quad x \in \Omega, \quad t > 0, \quad \text{where} \quad \mathcal{W} = \begin{pmatrix} h \\ hu \end{pmatrix},$$

$$\mathcal{F}(\mathcal{W}) = \begin{pmatrix} hu \\ hu^2 + \frac{1}{2}\mathsf{g}h^2 \end{pmatrix}. \tag{6}$$

3.1.1. Well-posedness analysis

In this section, we demonstrate the well-posedness of (5) using the energy method. (See [23,24] for further information on the energy method.) To this end, we linearize, symmetrize (5) (see Appendix A) and freeze the coefficients, and arrive at

$$w_t + A w_x + B w_y = 0, \quad (x, y) \in \Omega, \quad t > 0, \tag{7}$$

where

$$w=\begin{pmatrix} g\tilde{h}/c\\ \tilde{u}\\ \tilde{v}\end{pmatrix},\quad A=\begin{pmatrix}u_0 & c & 0\\ c & u_0 & 0\\ 0&0&u_0\end{pmatrix},\quad B=\begin{pmatrix}v_0&0&c\\0&v_0&0\\c&0&v_0\end{pmatrix}.$$

The variables $\tilde{h}$, $\tilde{u}, \tilde{v}$, represent perturbations of the height and velocities. Also, u_0, v_0 and h_0 are the constant mean velocities and the height. Furthermore, $c=\sqrt{gh_0}$ is the gravity wave speed.

Applying the energy method on (7), leads to

$$\int_{\Omega} w^T w_t dxdy + \int_{\Omega}(w^T Aw)_x dxdy + \int_{\Omega}(w^T Bw)_y dxdy = 0. \tag{8}$$

Using the Green–Gauss theorem on (8) yields

$$\|w\|_t^2 + \oint_{\partial\Omega} w^T[(A,B)\cdot\hat{\mathbf{n}}]w ds = 0, \tag{9}$$

where $\hat{\mathbf{n}} = (\hat{n}_1,\hat{n}_2)$ denotes the outward unit normal vector of $\partial\Omega$; $(A,B)\cdot\hat{\mathbf{n}} = \hat{n}_1 A + \hat{n}_2 B$ and s is the coordinate along $\partial\Omega$.

First, we consider the computational domain $\Omega = [0,L_1]\times[0,L_2]$. At $x=\{0,L_1\}$, $\hat{\mathbf{n}} = \pm e_1$ and at $y=\{0,L_2\}$, $\hat{\mathbf{n}}=\pm e_2$. We recast (9) as

$$\begin{aligned}\|w(t,x,y)\|_t^2 = \int_{x=0} w^T Aw dy - \int_{x=L_1} w^T Aw dy\\ + \int_{y=0} w^T Bw dx - \int_{y=L_2} w^T Bw dx.\end{aligned} \tag{10}$$

To obtain a bound on the solution w, the right-hand side of (10) must be bounded with appropriate boundary conditions. However, different flow conditions require different boundary conditions, see Appendix B.

3.2. *Curvilinear Shallow Water Equations*

We begin by briefly summarizing the mapping of the SWE from a Cartesian to a curvilinear coordinate frame. Let

$$x = x(\xi,\eta), \quad \text{and} \quad y = y(\xi,\eta), \tag{11}$$

be the mapping from $\Omega_{\bar{\xi}}(\xi,\eta)$: $[0,1]\times[0,1]$ to Ω. We have the following metric relations:

$$\mathcal{J}\xi_x = y_\eta, \quad \mathcal{J}\eta_x = -y_\xi, \tag{12}$$

$$\mathcal{J}\xi_y = -x_\eta, \quad \mathcal{J}\eta_y = x_\xi, \tag{13}$$

and $\mathcal{J} = x_\xi y_\eta - x_\eta y_\xi$ which denotes the determinant of the metric Jacobian.

The curvilinear form of the SWE are

$$(\mathcal{J}\mathcal{W})_t + F_\xi + G_\eta = 0, \tag{14}$$

where $F = (\mathcal{J}\xi_x\mathcal{F} + \mathcal{J}\xi_y\mathcal{G})$ and $G = (\mathcal{J}\eta_x\mathcal{F}+\mathcal{J}\eta_y\mathcal{G})$ expressed respectively as:

$$\mathcal{J}\begin{pmatrix}\xi_x hu + \xi_y hv\\ \xi_x hu^2 + \xi_x gh^2/2 + \xi_y huv\\ \xi_x huv + \xi_y hv^2 + \xi_y gh^2/2\end{pmatrix} \quad \text{and} \quad \mathcal{J}\begin{pmatrix}\eta_x hu + \eta_y hv\\ \eta_x hu^2 + \eta_x gh^2/2 + \eta_y huv\\ \eta_x huv + \eta_y hv^2 + \eta_y gh^2/2\end{pmatrix}.$$

We term (14) as the Curvilinear Shallow Water Equations (CSWE). The linear and symmetric form of (14) then becomes,

$$(\mathcal{J}w)_t + (\hat{A}w)_\xi + (\hat{B}w)_\eta = 0, \tag{15}$$

where the new jacobian matrices are $\hat{A} = A\mathcal{J}\xi_x + B\mathcal{J}\xi_y$ and $\hat{B} = A\mathcal{J}\eta_x + B\mathcal{J}\eta_y$. This is a standard procedure and, therefore, only briefly explained. For similar derivations, see [13,25–28].

3.2.1. *Well-posedness*

Since the computational domain, $\Omega_{\bar{\xi}}$ is a square, we replace the matrices A and B in Section 3.1.1 with $\hat{A}$ and $\hat{B}$ for the well-posedness analysis. In the curvilinear frame, the derivations regarding x and y turn to be ξ and η. We obtain

$$\begin{aligned}\|\sqrt{\mathcal{J}}w\|_t^2 = \int_{\xi=0} w^T\hat{A}wd\eta - \int_{\xi=1} w^T\hat{A}wd\eta + \int_{\eta=0} w^T\hat{B}wd\xi\\ - \int_{\eta=1} w^T\hat{B}wd\xi.\end{aligned} \tag{16}$$

As before, we focus on one boundary term, $\xi=0$. This reduces (16) to

$$\|\sqrt{\mathcal{J}}w\|_t^2 = \int_{\xi=0} w^T\hat{A}wd\eta, \qquad \text{where} \quad \hat{A} = A\mathcal{J}\xi_x + B\mathcal{J}\xi_y. \tag{17}$$

Let $\mathbf{n} = (n_1,n_2) = \mathcal{J}(\xi_x,\xi_y)$ (at $\xi=0$), which is normal to the boundary (not necessarily of unit length but that is of no importance here). Then, from (17), we have

$$\hat{A} = An_1 + Bn_2 = \begin{pmatrix}u_0n_1+v_0n_2 & cn_1 & cn_2\\ cn_1 & u_0n_1+v_0n_2 & 0\\ cn_2 & 0 & u_0n_1+v_0n_2\end{pmatrix}. \tag{18}$$

Keeping in mind that all other non-unit normal at the other boundaries are given as

$$\begin{aligned}&(n_1,n_2) = \mathcal{J}(\xi_x,\xi_y) \quad (\text{at} \quad \xi=1) \quad \text{and} \quad (n_1,n_2) = \mathcal{J}(\eta_x,\eta_y)\\ &(\text{at} \quad \eta=0,\eta=1).\end{aligned} \tag{19}$$

3.2.2. *Boundary conditions*

From the above derivation, it is clear that the curvilinear far-field conditions are completely analogous to the Cartesian case in Proposition 5. Simply exchange A, B with $\hat{A}, \hat{B}$.

We summarize the far-field boundary conditions for (15) in the following proposition:

Proposition 1. *Let* $R_1^T\hat{A}R_1 = \Lambda_1$ *and* $R_2^T\hat{B}R_2 = \Lambda_2$ *where* $\Lambda_{1,2} = diag((u_0,v_0)\cdot\mathbf{n}, (u_0,v_0)\cdot\mathbf{n}+c, (u_0,v_0)\cdot\mathbf{n}-c)$*, Then the far-field boundary conditions*

$$\begin{aligned}&\hat{A}^+w = \hat{A}^+g_1^f, \quad \xi=0, \qquad \hat{A}^-w = \hat{A}^-g_2^f, \quad \xi=1,\\ &\hat{B}^+w = \hat{B}^+g_3^f, \quad \eta=0, \qquad \hat{B}^-w = \hat{B}^-g_4^f, \quad \eta=1,\end{aligned}$$

lead to well-posedness of (15)*, where* $g_i^f, i=1,\dots,4$*, are known bounded functions.*

Similarly, by inserting the no-penetration boundary condition, $u_0n_1+v_0n_2 = 0$ at the boundary $\xi=0$, we obtain $\hat{A} = \begin{pmatrix}0 & cn_1 & cn_2\\ cn_1 & 0 & 0\\ cn_2 & 0 & 0\end{pmatrix}$. From (17), $w^T\hat{A}w = 2g(n_1\tilde{u}+n_2\tilde{v})\tilde{h}$ where $w = (g\tilde{h}/c,\tilde{u},\tilde{v})^T$ and setting $n_1\tilde{u}+n_2\tilde{v} = 0$, we obtain $\|\sqrt{\mathcal{J}}w\|_t^2 = 0$. The results are summarized in a proposition as follows:

Proposition 2. *The curvilinear Shallow Water Equations* (15) *is well-posed at* $\xi = \{0,1\}$ *and* $\eta = \{0,1\}$*, respectively, with wall boundary conditions* $(u_0n_1+v_0n_2) = 0$*, where the normals are given in* (19)*.*

4. Semi-discrete problem

With a 1-D computational grid set up in place and a scalar grid function $u(t) = u_i(t)$, see Section 2, we introduce the vectors $e_0 = (1,0,0,\dots,0)^T$, $e_1 = (0,0,0,\dots,1)^T$, and the matrices $E_0 = e_0e_0^T$ and $E_1 = e_1e_1^T$. Also, we define $D = P^{-1}Q$ as the spatial first-derivative finite-difference summation-by-parts (SBP) operator, which is (s,p)-accurate, if its truncation error is $T = (\mathcal{O}(\mathrm{h}^s),\dots,\mathcal{O}(\mathrm{h}^s),\mathcal{O}(\mathrm{h}^p),\dots,\mathcal{O}(\mathrm{h}^p),\mathcal{O}(\mathrm{h}^s),\dots,\mathcal{O}(\mathrm{h}^s))^T$, where $s<p$, see [29,30]. Here, P is a diagonal positive definite symmetric matrix, with entries scaled by the stepsize h and it also defines a discrete L_2-equivalent norm, $\|u\|^2 = u^TPu$. Also, $Q+Q^T = E_1 - E_0 = diag(-1,0,\dots,0,1)$. For first-order energy-stable hyperbolic problems, like (7), this leads to a convergence rate of $s+1$, see [31,32]. We refer readers to see [33,34] for a review of SBP schemes.

With the help of Kronecker products, denoted as $\otimes$, we extend the (scalar and 1-D) finite-difference operator to systems of equations and higher dimensional problems, see [35,36] for definitions and properties. To define the schemes for (5), we follow the approach in [25,26] for the Navier–Stokes equations. We introduce a 2-D grid with $(M+1)$ points along the x-axis and $(N+1)$ points along the y-axis and denote the numerical solution as

$$\mathcal{V}(t) = [\mathcal{V}_{001},\mathcal{V}_{002},\mathcal{V}_{003},\mathcal{V}_{101},\mathcal{V}_{102},\mathcal{V}_{103},\dots,\mathcal{V}_{MN1},\mathcal{V}_{MN2},\mathcal{V}_{MN3}]^T, \tag{20}$$

where $\mathcal{V}_{ijk} = \mathcal{V}(t)_{ijk}$ $(i \in (0,\dots,M)$, $j \in (0,\dots,N)$ and $k \in (1,2,3))$ denotes the numerical approximation of $\mathcal{W}_k(t,x_i,y_j)$, that is kth component of $\mathcal{W}$ at x_i, y_j.

We can now define SBP operators for a system with three variables in 2-D as

$$\mathbf{D}_x = (I_y \otimes D_x \otimes I_3), \quad \mathbf{D}_y = (D_y \otimes I_x \otimes I_3), \tag{21}$$

where $D_{x,y} = P_{x,y}^{-1} Q_{x,y}$, respectively, denote the differentiation operators in the $\{x,y\}$-directions. In all the Kronecker products, matrices in first place have size $(N+1)\times(N+1)$, the second place are of size $(M+1)\times(M+1)$ and the third place is a 3×3 identity matrix. In the same way, we define the norm (or integration) matrices

$$\mathbf{P}_x = (I_y \otimes P_x \otimes I_3), \quad \mathbf{P}_y = (P_y \otimes I_x \otimes I_3), \quad \mathbf{P} = \mathbf{P}_x\mathbf{P}_y = (P_y \otimes P_x \otimes I_3),$$

and the restriction matrices

$$\mathbf{E}_{0x} = (I_y \otimes E_0 \otimes I_3), \quad \mathbf{E}_{1x} = (I_y \otimes E_1 \otimes I_3),$$
$$\mathbf{E}_{0y} = (E_0 \otimes I_x \otimes I_3), \quad \mathbf{E}_{1y} = (E_1 \otimes I_x \otimes I_3).$$

We assume that E_0 and E_1 have the appropriate sizes. Also, we consider the discrete norm defined in (4).

Analogously to (20), we define the discrete flux vectors, $\bar{\mathcal{F}}, \bar{\mathcal{G}}$ with components $\bar{\mathcal{F}}_{kij}, \bar{\mathcal{G}}_{kij}$. Furthermore, $\bar{g}$ is the discrete boundary data with the same structure as the discrete fluxes. The form of $\bar{g}$ with (far-field/wall) boundary data vector projected at $x = 0$ have entries given by

$$\bar{g}_{ij}(t) = \begin{cases} g(t,x_i,y_j) & \text{for} \quad i = 0, \forall j, \\ 0 & \text{otherwise.} \end{cases} \tag{22}$$

Here, $g(t,x_i,y_j)$ is the boundary vector function (data) evaluated at (i,j)th discrete point. Note, we will use f or w as a superscript on $\bar{g}$ to represent far-field or wall boundary data when appropriate.

4.1. Stability of the Curvilinear Shallow Water Equations

All vectors and matrices are defined as in the Cartesian case, but the indices i,j now refer to the computational coordinates ξ_i, η_j. A semi-discrete approximation of (14) is

$$(\bar{\mathcal{J}}\mathcal{V})_t + \mathbf{D}_\xi \bar{\mathcal{F}} + \mathbf{D}_\eta \bar{\mathcal{G}} = \mathsf{S}(\mathcal{V}, \bar{g}). \tag{23}$$

After linearizing and symmetrizing (23) becomes

$$(\bar{\mathcal{J}}v)_t + \mathbf{D}_\xi(\hat{\mathbf{A}}v) + \mathbf{D}_\eta(\hat{\mathbf{B}}v) = \mathsf{S}(v, \bar{g}). \tag{24}$$

We perform the energy analysis and apply the SBP properties to obtain

$$\|\sqrt{\bar{\mathcal{J}}}v\|_t^2 - v^T\mathbf{P}_\eta\mathbf{E}_{0\xi}(\hat{\mathbf{A}}v) + v^T\mathbf{P}_\eta\mathbf{E}_{1\xi}(\hat{\mathbf{A}}v) - v^T\mathbf{P}_\xi\mathbf{E}_{0\eta}(\hat{\mathbf{B}}v) + v^T\mathbf{P}_\xi\mathbf{E}_{1\eta}(\hat{\mathbf{B}}v)$$
$$= 2v^T\mathbf{P}\mathsf{S}(v, \bar{g}), \tag{25}$$

just as in (Appendix C). Here, the energy statement (25) corresponds to a discrete equivalent of (16).

4.1.1. Discrete far-field boundary conditions

With focus on $\xi = \xi_0$, we propose the penalty term

$$\mathsf{S}_{\xi_0}(v, \bar{g}^f) = -\mathbf{P}_\xi^{-1}\mathbf{E}_{0\xi}\hat{\mathbf{A}}^+(v - \bar{g}^f). \tag{26}$$

Substituting (26) into (25), we arrive at

$$\|\sqrt{\bar{\mathcal{J}}}v\|_t^2 - v^T\mathbf{P}_\eta\mathbf{E}_{0\xi}(\hat{\mathbf{A}}v) = -2v^T\mathbf{P}_\eta\mathbf{E}_{0\xi}\hat{\mathbf{A}}^+(v - \bar{g}^f).$$

As before, we decompose the matrix $\hat{\mathbf{A}}$ into positive and negative parts and drop the terms that do not contribute to the energy growth rate,

$$\|\sqrt{\bar{\mathcal{J}}}v\|_t^2 \leq \left(v^T\mathbf{P}_\eta\mathbf{E}_{0\xi}(\hat{\mathbf{A}}^+)v - 2v^T\mathbf{P}_\eta\mathbf{E}_{0\xi}\hat{\mathbf{A}}^+(v - \bar{g}^f)\right), \tag{27}$$

and recast it as,

$$\|\sqrt{\bar{\mathcal{J}}}v\|_t^2 \leq \quad \left(-(v - \bar{g}^f)^T\mathbf{P}_\eta\mathbf{E}_{0\xi}\hat{\mathbf{A}}^+(v - \bar{g}^f) + \bar{g}^{fT}\mathbf{P}_\eta\mathbf{E}_{0\xi}\hat{\mathbf{A}}^+\bar{g}^f\right). \tag{28}$$

The RHS of (28) is bounded with the last term representing the energy sent across the boundary $\xi = \xi_0$ into the domain. The results are summarized in the proposition below:

Proposition 3. *Given the discrete version of the preamble in Proposition 1, the following penalty (SAT) terms lead to the stability of the scheme (24):*

$$-\mathbf{P}_\xi^{-1}\mathbf{E}_{0\xi}\hat{\mathbf{A}}^+(v - \bar{g}_1^f), \quad \xi = \xi_0, \quad \mathbf{P}_\xi^{-1}\mathbf{E}_{1\xi}\hat{\mathbf{A}}^-(v - \bar{g}_2^f), \quad \xi = \xi_M,$$
$$-\mathbf{P}_\eta^{-1}\mathbf{E}_{0\eta}\hat{\mathbf{B}}^+(v - \bar{g}_3^f), \quad \eta = \eta_0, \quad \mathbf{P}_\eta^{-1}\mathbf{E}_{1\eta}\hat{\mathbf{B}}^-(v - \bar{g}_4^f), \quad \eta = \eta_N,$$

where $\bar{g}_l^f, l = 1,\dots,4$ is boundary data projected at a boundary and, depending on its position, takes entries defined similarly to (22).

4.1.2. Discrete wall boundary conditions

Similar to the Appendix C.2, we propose a penalty term (SAT)

$$\mathsf{S}_{\xi_0}(v, \bar{g}^w) = -2\mathbf{P}_\xi^{-1}\mathbf{E}_{0\xi}\hat{\mathbf{A}}^+(v - \bar{g}^w), \tag{29}$$

at the wall boundary. Substituting (29) into (25) with focus on $\xi = \xi_0$ yields

$$\|\sqrt{\bar{\mathcal{J}}}v\|_t^2 - v^T\mathbf{P}_\eta\mathbf{E}_{0\xi}(\hat{\mathbf{A}}v - 4\hat{\mathbf{A}}^+(v - \bar{g}^w)) = 0.$$

Next, we focus on the construction of $\bar{g}^w$ at a boundary point (ξ_0, η_j). No flow through the boundary implies that both $(\mathbf{u}\cdot\mathbf{n})\mathbf{n} = 0$ and $(\tilde{\mathbf{u}}\cdot\mathbf{n})\mathbf{n} = 0$. The first condition goes into the matrix $\hat{\mathbf{A}}$ and the second is used to construct $\bar{g}$ at (ξ_0, η_j)th boundary point. Now in complete analogy with the Cartesian case, the continuous boundary data function is $g^w = (\mathrm{g}\tilde{h}/c, \tilde{u} - (\tilde{\mathbf{u}}\cdot\mathbf{n})n_1, \tilde{v} - (\tilde{\mathbf{u}}\cdot\mathbf{n})n_2)^T$.

For stability of the semi-discrete problem, we must show that

$$v^T\mathbf{P}_\eta\mathbf{E}_{0\xi}(\hat{\mathbf{A}}v - 4\hat{\mathbf{A}}^+(v - \bar{g}^w)) \leq 0. \tag{30}$$

Just as in the Cartesian case, we rewrite (30) in component form

$$\sum_j v_{0j}^T P_{\eta j}(\hat{A}v_{0j} - 4\hat{A}^+(v_{0j} - \bar{g}_{0j}^w)) \leq 0. \tag{31}$$

We insert the wall boundary condition $u_0n_1 + v_0n_2 = 0$ into $\hat{A}$ and $\hat{A}^+$, and consider one term of (31)

$$\begin{aligned} v^T\hat{A}v - 4v^T\hat{A}^+(v - \bar{g}^w) &= 2\mathrm{g}n_1\tilde{h}\tilde{u} + 2\mathrm{g}n_2\tilde{h}\tilde{v} - 2\mathrm{g}n_1\tilde{h}\tilde{u} \\ &\quad - 2\mathrm{g}n_2\tilde{h}\tilde{v} - 2n_1^2c\tilde{u}^2 - 4n_1n_2c\tilde{u}\tilde{v} - 2n_2^2c\tilde{v}^2 \\ &= -2n_1^2c\tilde{u}^2 - 4n_1n_2c\tilde{u}\tilde{v} - 2n_2^2c\tilde{v}^2 \\ &= -2c(n_1\tilde{u} + n_2\tilde{v})^2 \leq 0. \end{aligned}$$

Hence, the stability proof of bounded solution when wall boundary condition is imposed. □

We summarize the results for all other boundaries in the following proposition.

Proposition 4. *Let $\bar{g}_l^w, l = 1,\dots,4$ be the boundary data projected at the boundary. Then the following penalty (SAT) terms,*

$$-2\mathbf{P}_\xi^{-1}\mathbf{E}_{0\xi}\hat{\mathbf{A}}^+(v - \bar{g}_1^w), \quad \xi = \xi_0, \quad 2\mathbf{P}_\xi^{-1}\mathbf{E}_{1\xi}\hat{\mathbf{A}}^-(v - \bar{g}_2^w), \quad \xi = \xi_M,$$
$$-2\mathbf{P}_\eta^{-1}\mathbf{E}_{0\eta}\hat{\mathbf{B}}^+(v - \bar{g}_3^w), \quad \eta = \eta_0, \quad 2\mathbf{P}_\eta^{-1}\mathbf{E}_{1\eta}\hat{\mathbf{B}}^-(v - \bar{g}_4^w), \quad \eta = \eta_N,$$

lead to stability of the scheme (24).

5. Numerical experiments

We have implemented the numerical scheme (23) with (26) and (29). We use SBP operators of order $2s$ in the interior and order s close to the spatial boundaries (denoted SBP$(s,2s)$), where $s \in \{1,2,3\}$ [13,23,34]. We march in time with the standard 4th-order Runge Kutta scheme and use a CFL number of 0.50 in all the simulations. The $\mathbf{A}^{+,-}$ matrices in the SAT's are evaluated using the associated boundary-data vector $\bar{g}$.

Whenever an exact solution is available, one can compute the errors using the L^2 norm defined in (4)

$$\|\mathbf{e}\|_{\mathbf{P}} = \sqrt{\mathbf{e}^T\mathbf{P}\mathbf{e}},$$

Table 1
The rates of convergence and errors at $T = 1.0$ for height under a mesh refinement sequence.

Grid points	SBP(1, 2)		SBP(2, 4)		SBP(3, 6)	
	r	L^2 error	r	L^2 error	r	L^2 error
50	–	0.0049	–	4.2269×10^{-4}	–	1.6532×10^{-4}
100	2.0299	0.0012	3.0458	5.1185×10^{-5}	4.0167	1.0214×10^{-5}
200	2.0111	2.9621×10^{-4}	3.0203	6.3087×10^{-6}	3.9607	6.5596×10^{-7}
400	2.0033	7.3881×10^{-5}	3.0060	7.8533×10^{-7}	3.9319	4.2978×10^{-8}

Table 2
The rates of convergence and errors at $T = 1.0$ for momentum under a mesh refinement sequence.

Grid points	SBP(1, 2)		SBP(2, 4)		SBP(3, 6)	
	r	L^2 error	r	L^2 error	r	L^2 error
50	–	0.0037	–	3.1666×10^{-4}	–	1.9787×10^{-4}
100	2.0258	9.0348×10^{-4}	3.0370	3.8581×10^{-5}	4.0036	1.2336×10^{-5}
200	2.0106	2.2422×10^{-4}	3.0117	4.7837×10^{-6}	3.9816	7.8091×10^{-7}
400	2.0036	5.5915×10^{-5}	2.9984	5.9865×10^{-7}	3.9624	5.0097×10^{-8}

Table 3
The rates of convergence and errors at $T = 1.0$ for height h under a mesh refinement sequence.

Grid points	SBP(1, 2)		SBP(2, 4)		SBP(3, 6)	
	r	L^2 error	r	L^2 error	r	L^2 error
25	–	0.0084	–	0.0015	–	0.0021
50	1.9736	0.0021	2.9898	1.8895×10^{-4}	4.0045	1.3084×10^{-4}
75	1.9361	9.5783×10^{-4}	2.9709	5.6650×10^{-5}	3.9988	1.1878×10^{-5}
100	1.9872	5.4077×10^{-4}	2.9559	2.4204×10^{-5}	4.0670	8.0254×10^{-6}

Table 4
The rates of convergence and errors at $T = 1.0$ for momentum hu under a mesh refinement sequence.

Grid points	SBP(1, 2)		SBP(2, 4)		SBP(3, 6)	
	r	L^2 error	r	L^2 error	r	L^2 error
25	–	0.0205	–	0.0015	–	0.0061
50	2.0945	0.0048	3.0561	0.0031	3.9650	3.9061×10^{-4}
75	2.0097	0.0021	3.0979	1.0614×10^{-4}	3.9713	7.8061×10^{-5}
100	1.9841	0.0012	3.0685	4.3904×10^{-5}	4.0112	2.4620×10^{-5}

Table 5
The rates of convergence and errors at $T = 1.0$ for momentum hv under a mesh refinement sequence.

Grid points	SBP(1, 2)		SBP(2, 4)		SBP(3, 6)	
	r	L^2 error	r	L^2 error	r	L^2 error
25	–	0.0101	–	0.0032	–	0.0016
50	1.9578	0.0026	3.0618	3.8323×10^{-4}	4.0341	3.7234×10^{-4}
75	2.0131	0.0011	3.0513	1.1085×10^{-4}	3.9907	7.3827×10^{-5}
100	2.0023	6.1834×10^{-4}	3.0881	2.3054×10^{-5}	4.0458	2.3054×10^{-5}

where $\mathbf{e}$ is the vector of the pointwise difference between the exact and the approximate solution.

The rate of convergence r is given by

$$r = \frac{\log(\|\mathbf{e}_1\|_{\mathbf{P}_1}/\|\mathbf{e}_2\|_{\mathbf{P}_2})}{\log((M+1)/(N+1))},$$

where the subscripts $\{1,2\}$ represent two different mesh sizes with $(M_{1,2}+1)\cdot(N_{1,2}+1)$ grid points respectively. Also, $\mathbf{e}_1$ and $\mathbf{e}_2$ are the errors with grid spacing h_1 and h_2, respectively. See [30–32,37] for more details on the order of accuracy of the initial boundary value problem.

5.1. Convergence rate for 1-D Swallow Water Equations with far-field boundaries

Here, we use the scheme given in (C.1) (reduced to 1-D) on the domain $[0,1]$ with far-field boundary conditions (see Proposition 7) on both ends of the domain. The function

$$\mathcal{W} = (h, hu) = [2+\sin(5x-10t), 2+\sin(5x-10t)]^T, \tag{32}$$

solves (6) if the additional source term

$$\mathcal{S} = [-\cos(5x-10t), (10\mathrm{g}-5)\cos(5x-10t)+5\mathrm{g}\sin(5x-10t)\cos(5x-10t)]^T,$$

is added to the right-hand side. This procedure is known as the “method of manufactured solutions”, see [21,22]. Adding a forcing function does not affect the stability proof, see [13]. From (32), we deduce the initial data f (at $t=0$) and time-dependent boundary data g (at $x=0$ and $x=1$).

We compute the solution on grids with $N = 50, 100, 200, 400$ spatial nodes. The errors are computed at $T = 1.0$. The rates of convergence for height and momentum are shown in Tables 1 and 2, respectively. We use the SBP schemes of order $(1,2), (2,4)$ and $(3,6)$ with theoretical convergence rates of order 2, 3, and 4, respectively. As expected, we obtained the desired order for the numerical simulations of 1-D SWE in all three cases in agreement with our analysis.

We also consider simulations of the 1-D model with manufactured solution (32) for a longer time. The errors until $T = 40$ with 100 grid points are presented in Fig. 1. In Fig. 1, we observe a bounded error growth with respect to time in agreement with [38].

5.1.1. Convergence rates for Curvilinear Shallow Water Equations with far-field boundaries

Next, we turn to the Curvilinear Shallow Water Equations where we examine the scheme given in (23) with far-field boundary conditions at all boundaries (see Proposition 3). We consider a circular bend domain (see Fig. 2a). In polar coordinates, the circular bend is given as $\Omega_{\xi}(r,\theta) = [0.5,1]\times[0.2,2]$. We use the manufactured solution

$$\mathcal{W} = [2+\sin(5x+5y-10t), 2+\sin(5x+5y-10t), 2+\sin(5x+5y-10t)]^T \tag{33}$$

and the additional source term

$$\begin{aligned}\mathcal{S} = \mathcal{J}[&0, 10\mathrm{g}\sin(5x+5y-10t)+5\mathrm{g}\sin(5x+5y-10t)\cos(5x+5y-10t),\\ &10\mathrm{g}\sin(5x+5y-10t)\\ &+5\mathrm{g}\sin(5x+5y-10t)\cos(5x+5y-10t)]^T.\end{aligned}$$

We compute the solution on equidistant $N\times N$ grids in (ξ,η), where $N = 25, 50, 75, 100$. The initial data f and boundary data g are deduced from the (33). Errors and rates of convergence for the conserved variables at time $T = 1.0$ are computed for the circular domain and displayed in Tables 3–5. We show in Fig. 2b the solution at $T = 1.0$ on both domains obtained with SBP(3, 6). The numerical experiments on these grids show the robustness of the CSWE scheme on a more general domain.

5.1.2. Convergence rates for Curvilinear Shallow Water Equations with wall boundaries

Next, we demonstrate the imposition of wall boundary conditions (see Proposition 4) on our circular bend by using the manufactured solution given by

$$\mathcal{W} = [2+\sin(5x+5y-10t), 0, 0]^T, \tag{34}$$

and manufactured source term

$$\begin{aligned}\mathcal{S} = \mathcal{J}&\cos(5x+5y-10t)[-10, 5\mathrm{g}(2+\sin(5x+5y-10t)),\\ &5\mathrm{g}(2+\sin(5x+5y-10t))]^T.\end{aligned}$$

Remark 1. Note that although the solution is zero for hu and hv, the corresponding fluxes are not trivial, due to the forcing term.

From (34), we deduce the initial data f and time-dependent boundary data g. Errors and rates of convergence are given in Tables 6–8. Furthermore, we show in Fig. 3 the momentum field at time $T = 1.0$

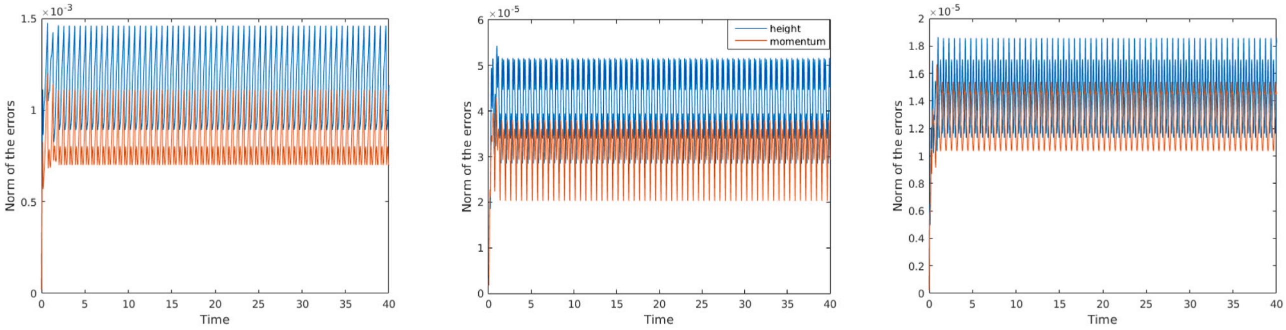

(a) SBP(1,2) Scheme (b) SBP(2,4) Scheme (c) SBP(3,6) Scheme

Fig. 1. Long time simulation of 1-D SWE. The L^2 error for the height and momentum solution components versus time using 100 grid points.

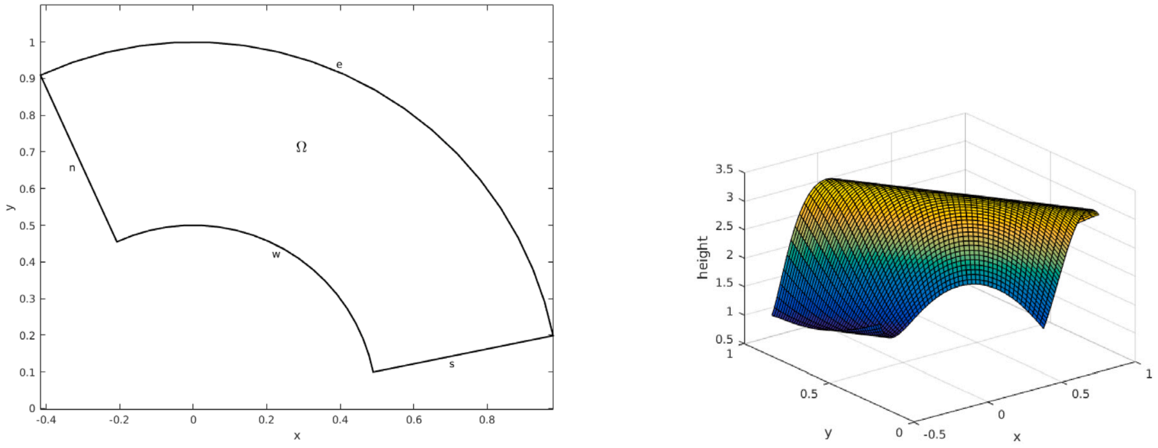

(a) (b)

Fig. 2. A schematic of a physical curvilinear domain in a Cartesian coordinate and Height solution at $T = 1.0$ in Curvilinear domains.

Table 6
The rates of convergence and errors at $T = 1.0$ for height h under a mesh refinement sequence.

Grid points	SBP(1, 2)		SBP(2, 4)		SBP(3, 6)	
	r	L^2 error	r	L^2 error	r	L^2 error
25	–	0.0081	–	0.0041	–	0.0052
50	1.9733	0.0021	3.0706	4.8802×10^{-4}	3.9161	3.4446×10^{-4}
75	2.0490	9.1498×10^{-4}	3.0418	1.4217×10^{-4}	3.9457	6.9556×10^{-5}
100	2.0289	5.1041×10^{-4}	3.0176	5.9675×10^{-5}	4.0139	2.1914×10^{-5}

Table 7
The rates of convergence and errors at $T = 1.0$ for momentum hu under a mesh refinement sequence.

Grid points	SBP(1, 2)		SBP(2, 4)		SBP(3, 6)	
	r	L^2 error	r	L^2 error	r	L^2 error
25	–	0.0146	–	0.0054	–	0.0094
50	1.9890	0.0037	2.9810	6.8395×10^{-4}	3.9741	5.9814×10^{-4}
75	1.9486	0.0017	3.0148	2.0144×10^{-4}	4.0173	1.1733×10^{-4}
100	1.9667	9.6545×10^{-4}	2.9086	8.7247×10^{-5}	4.0238	3.6817×10^{-5}

Table 8
The rates of convergence and errors at $T = 1.0$ for momentum hv under a mesh refinement sequence.

Grid points	SBP(1, 2)		SBP(2, 4)		SBP(3, 6)	
	r	L^2 error	r	L^2 error	r	L^2 error
25	–	0.0097	–	0.0068	–	0.0096
50	1.9191	0.0026	2.9690	8.6846×10^{-4}	3.9498	6.2125×10^{-4}
75	2.0197	0.0011	2.9118	2.6669×10^{-4}	3.9657	1.2442×10^{-4}
100	2.0303	9.4795×10^{-4}	3.0301	1.1026×10^{-4}	4.0246	3.9090×10^{-5}

obtained with SBP(3, 6). Note how the trajectories are aligned with the wall in agreement with the no-penetration boundary condition. This plot is zoomed in at various corners of the domain to allow a clearer view of the behaviour of the solution.

5.2. *Applications*

Testing the schemes on more realistic problems, we consider the propagation of a flood wave in a stream, river or open channel. Predicting such flows is of great practical use, as it can be used in early flood warning systems. Here, we consider three examples of such flows: a 1-D and a 2-D river flow in a channel and a dam-break simulation.

5.2.1. *Steady river channel*

Next, we consider the domain $[0, 1]$ as a 1-D model of a river. This case is designed to stress-test the open boundary condition. We initiate the simulation with a hump of water. The hump is given as a Gaussian curve centred at $x = 0.5$ and overlaid on a river at rest (initial velocity $u_0 = 0$) with height $h_0 = 1$. Hence, the initial height h is given by

$$h(x, 0) = h_0 + 0.5e^{(-250(x-0.5)^2)}, \qquad 0 \le x \le 1. \tag{35}$$

The initial velocity u is set to u_0. The gravitational constant is taken as $g = 1$. Fig. 4 shows a solution to the height and momentum observed at different time instances. In Fig. 5, (x, t)-space plots are shown. We observe two flood waves (or wavefronts) travelling in opposite directions with different wave speeds $(\pm\sqrt{gh_0})$. The characteristic far-field boundary conditions are implemented, and the flood waves leave the domain freely at the boundary after time $0.60s$ without causing any visible reflections at the boundaries. This demonstrates the efficacy

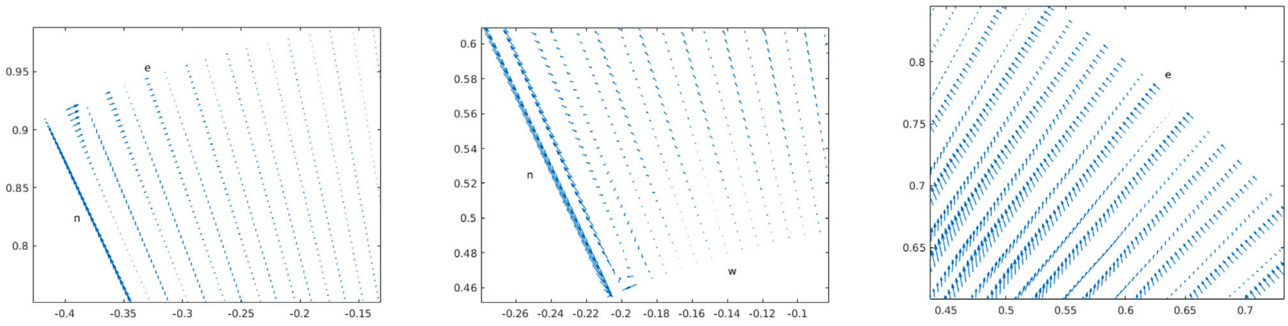

(a) zoom in of the momentum field at the North-East boundary

(b) zoom in of the momentum field at the North-West boundary

(c) zoom in of the momentum field at the West boundary

Fig. 3. Momentum field at time $T = 1.0$.

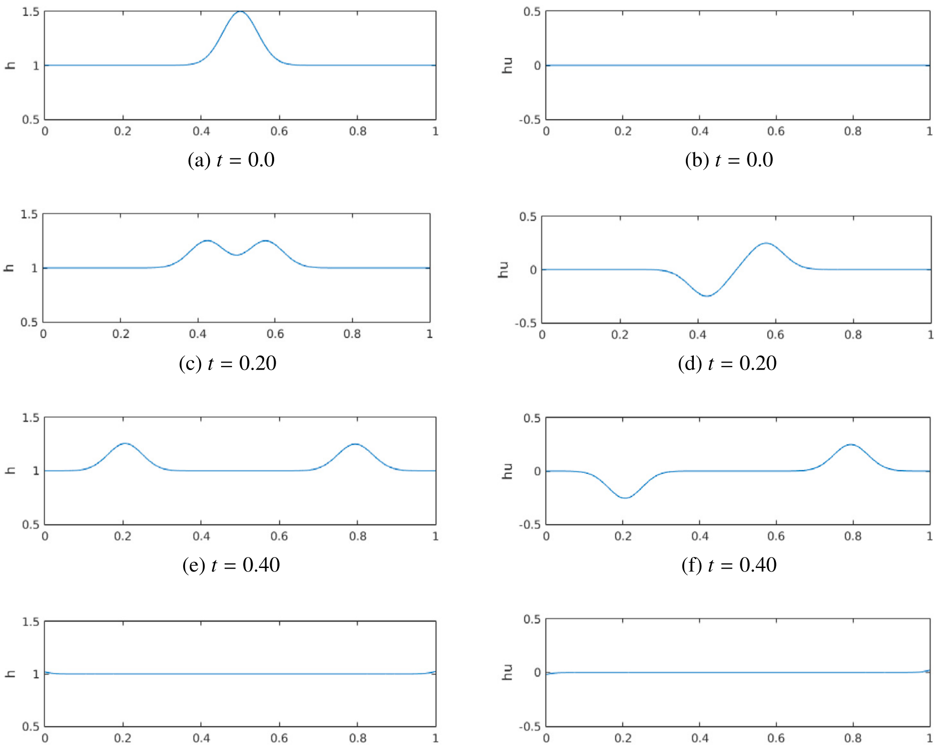

(a) $t = 0.0$

(b) $t = 0.0$

(c) $t = 0.20$

(d) $t = 0.20$

(e) $t = 0.40$

(f) $t = 0.40$

(g) $t = 0.60$

(h) $t = 0.60$

Fig. 4. Evolution of height and momentum concentrated at the centre. The small disturbance generates two waves propagating in both directions. The left column shows the height (h), and the right shows momentum (hu). Each row represents the height and momentum at different times $t = 0, 0.20, 0.40, 0.60$.

of the characteristic boundary conditions and the stability of the SAT implementation.

5.2.2. Flood control channel simulation

Next, we consider flood waves in a channel. Flood control channels are primarily situated in cities for conveying water or serving as a way to reduce flooding. They are usually built with erected wall structures along the sides, for example see Fig. 6.

We model a portion of a Cartesian and circular channel by imposing wall boundary conditions along the wall structures, shown in Fig. 7 and far-field boundary conditions at the open ends. We aim to show the robustness of the proposed wall boundary conditions from Section 4.1.2 and far-field boundary conditions from Section 4.1.1. To this end, we consider a flow with the initial velocity $(u, v) = (0, 0)$ and the initial height given by

$$h(x, y, 0) = 1 + 0.5e^{-25\left((x-0.5)^2+(y-0.5)^2\right)}, \tag{36}$$

In Figs. 8–10, we show the height and momentum in the Cartesian and circular domains at an instance in time $T = 1$. The flood waves have propagated to affect the flow in large parts of both domains. We also observe in the momentum field plots that, as flood waves move in a direction towards the wall structures, they deviate from moving along the wall towards the open boundaries. The SATs accurately and stably enforce the wall boundary conditions.

5.2.3. Dam break problem

Next, we examined another critical case which involves an area bounded by solid walls and a dam that separates a reservoir and a floodplain. Here, we demonstrate a 1-D domain bounded by walls at $x = [0, 1]$. The dam is broken instantly at time $t = 0$, which gives rise to the following discontinuous initial data

$$h(x, 0) = \begin{cases} 3; & \text{if} \quad x < 0.5 \\ 1; & \text{if} \quad x > 0.5 \end{cases} \qquad u(x, 0) = 0. \tag{37}$$

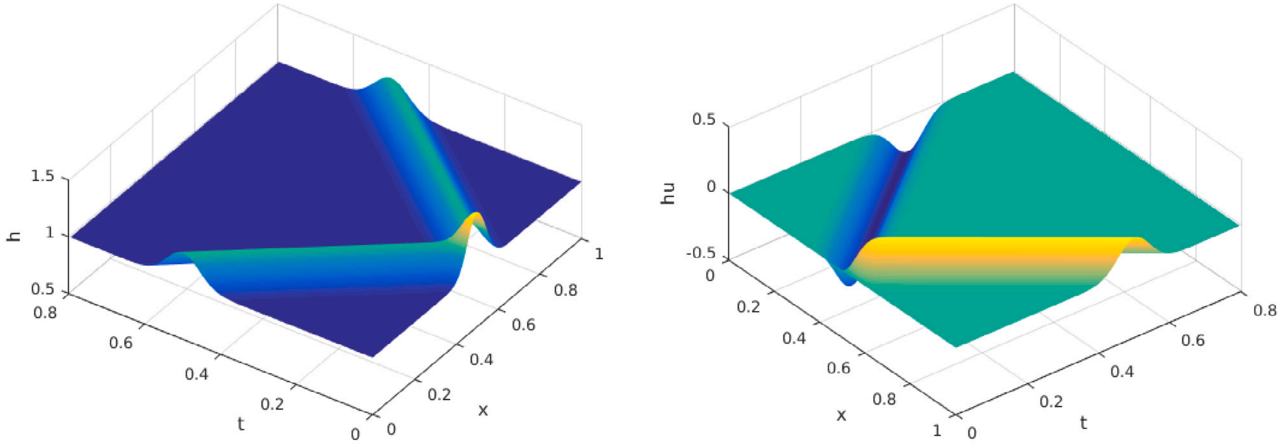

(a) water depth (or height)

(b) momentum

Fig. 5. (x,t)-space plot of Fig. 4 respectively.

Fig. 6. Flood control channel at Anloga junction in Kumasi, Ghana.

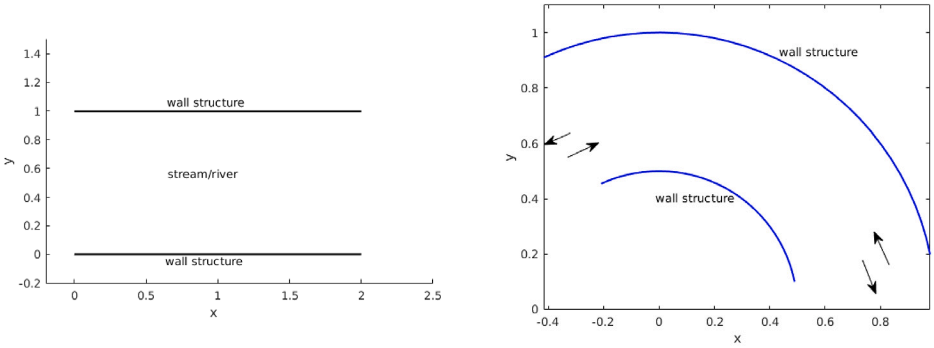

(a) Cartesian domain

(b) Curvilinear domain

Fig. 7. Planar view of the two channels considered in Section 5.2.2.

The domain $[0,1]$ is discretized with 100 grid points. The exact solution consists of a right-going shock and a left-going rarefaction. It is shown in Fig. 11 that the numerical solution behaves similarly. However, since our scheme lacks shock-capturing capabilities, we have large oscillations in the solutions of Fig. 11(a, b) caused by the discontinuity in the data. Nevertheless, the scheme is stable. In Fig. 11(c, d), we have added a little artificial diffusion, which yields a non-oscillatory solution. Here, we used a simple Laplacian-type artificial diffusion,

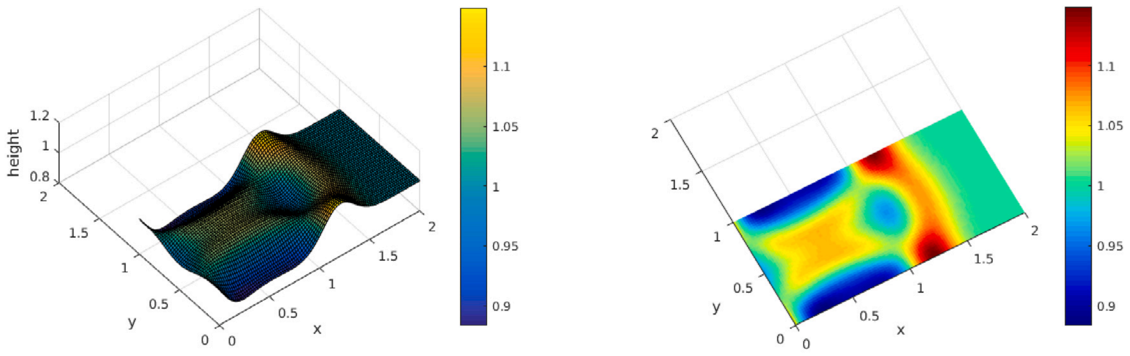

(a) Water depth (or height) at $T = 1.0$ (b) Planar view of water depth

Fig. 8. Plots of water depth at time $T = 1.0$.

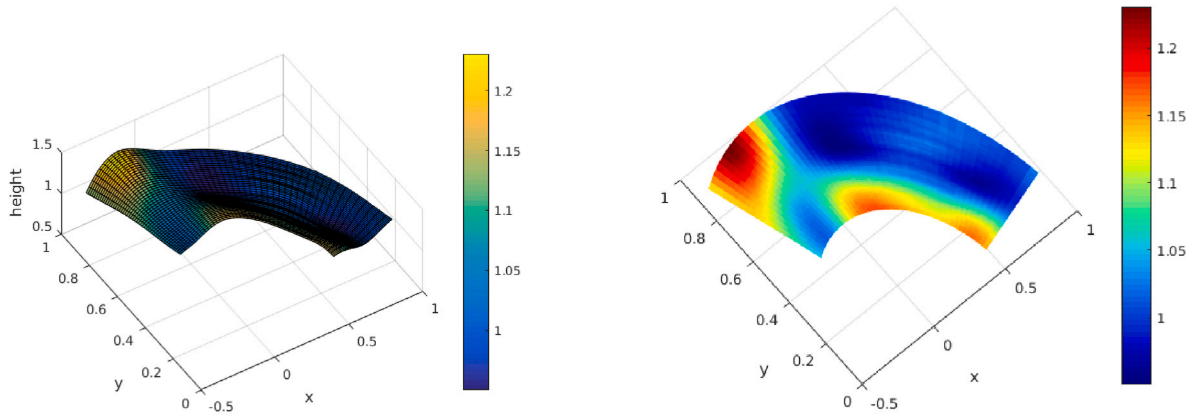

(a) Water depth (or height) at $T = 1.0$ (b) Planar view of water depth

Fig. 9. Plots of water depth at time $T = 1.0$.

which is tuned to control the oscillations for this particular example. However, the artificial diffusion requires further attention and since the focus here is on the boundary treatment we postpone the analysis of artificial diffusion to a future article. Note that in the previous smooth test cases, there are no oscillations in the solution despite no artificial diffusion added to the schemes. Furthermore, all outputs in Fig. 11 are stable with the boundary conditions.

6. Conclusions

The study carried out a continuous and semi-discrete energy estimate analysis to prove the well-posedness and stability of the Shallow Water Equations. Specifically, we re-derived the set of far-field boundary conditions. In particular, we considered the wall B.C. all in a matrix approach that is much simpler to work with than the component approach considered by [14]. We also provided stability proof for a Summation-by-Parts Simultaneous Approximation Term (SBP-SAT) scheme for far-field and wall boundary conditions. We also took into account the curvilinear generalization to a real domain.

These boundary conditions were implemented with a weak boundary procedure to obtain continuous energy estimates. Furthermore, high-order summation-by-parts finite-difference schemes were constructed for the SWE in both coordinate systems, including the well-posed open and wall boundary conditions on a single domain. We performed numerical computations with verifiable and correct convergence rates toward the exact solution using the method of manufactured solution. Subsequently, we conducted simulations to show the robustness of the boundary conditions for the SWE which had an oscillating solution and was therefore damped by the addition of artificial diffusion. It was observed that the simulated solution of these applications obeys the boundary conditions and confirms our analysis.

7. Declaration

Funding

No funding was received for conducting this study.

CRediT authorship contribution statement

Reindorf Nartey Borkor: Conceiving and planning the project, Formal analysis, Methodology, Carried out the implementation, Writing – original draft, Writing – review & editing. **Magnus Svärd:** Conceiving and planning the project, Formal analysis, Methodology, Writing – review & editing, Supervision. **Peter Amoako-Yirenkyi:** Conceiving and planning the project, Formal analysis, Methodology, Writing – review & editing, Supervision.

Declaration of competing interest

The authors declare that they have no known competing financial interests or personal relationships that could have appeared to influence the work reported in this paper.

Data availability

No data was used for the research described in the article.

Acknowledgement

We acknowledge the Directorate of the National Institute of Mathematical Science Ghana for the office space and resources made available for this study.

Appendix A. Linearization and symmetrization of 2-*D* Shallow Water Equations

We briefly present the process of obtaining linear, and symmetric Shallow Water Equations [19]. First, we rewrite the system (5) in quasi-linear form,

$$\mathcal{W}_t + \bar{A}\mathcal{W}_x + \bar{B}\mathcal{W}_y = 0, \tag{A.1}$$

where the Jacobian matrices $\bar{A}$ and $\bar{B}$ are

$$\bar{A} = \begin{pmatrix} 0 & 1 & 0 \\ -u^2 + gh & 2u & 0 \\ -uv & v & u \end{pmatrix}, \quad \bar{B} = \begin{pmatrix} 0 & 0 & 1 \\ -uv & v & u \\ -v^2 + gh & 0 & 2v \end{pmatrix}.$$

Next, we shift the variables from the conservative $\mathcal{W} = (h, hu, hv)^T$ to the primitive variables $\mathcal{U} = (h, u, v)^T$ using the transformation matrix

$$\mathcal{M} = \frac{\partial \mathcal{W}}{\partial \mathcal{U}} = \begin{pmatrix} 1 & 0 & 0 \\ u & h & 0 \\ v & 0 & h \end{pmatrix}. \tag{A.2}$$

We rewrite Eq. (A.1) as

$$\mathcal{W}_t + \mathcal{M}(\mathcal{M}^{-1}\bar{A}\mathcal{M})\mathcal{M}^{-1}\mathcal{W}_x + \mathcal{M}(\mathcal{M}^{-1}\bar{B}\mathcal{M})\mathcal{M}^{-1}\mathcal{W}_y = 0,$$

and introduce the following

$$\mathcal{A} = \mathcal{M}^{-1}\bar{A}\mathcal{M} = \begin{pmatrix} u & h & 0 \\ g & u & 0 \\ 0 & 0 & u \end{pmatrix}, \quad \mathcal{B} = \mathcal{M}^{-1}\bar{B}\mathcal{M} = \begin{pmatrix} v & 0 & h \\ 0 & v & 0 \\ g & 0 & v \end{pmatrix},$$

$$\mathcal{U}_t = \mathcal{M}^{-1}\mathcal{W}_t = \begin{pmatrix} h \\ u \\ v \end{pmatrix}_t, \quad \mathcal{U}_x = \mathcal{M}^{-1}\mathcal{W}_x = \begin{pmatrix} h \\ u \\ v \end{pmatrix}_x, \mathcal{U}_y = \mathcal{M}^{-1}\mathcal{W}_y = \begin{pmatrix} h \\ u \\ v \end{pmatrix}_y,$$

to obtain

$$\mathcal{U}_t + \mathcal{A}\mathcal{U}_x + \mathcal{B}\mathcal{U}_y = 0. \tag{A.3}$$

Eq. (A.3) is the non-linear non-conservation form of SWE (5) with primitive variables.

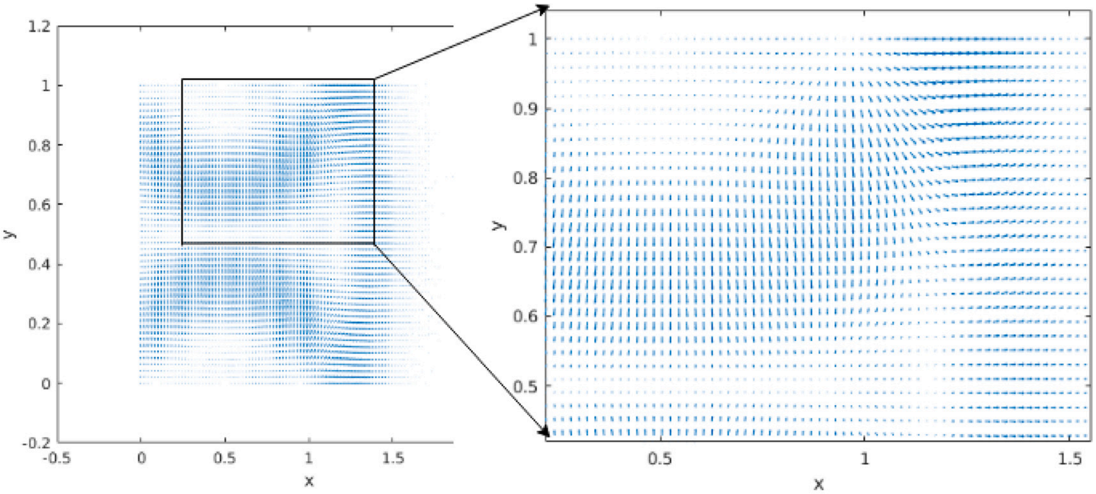

(a) Momentum field of the Cartesian domain at $T = 1.0$

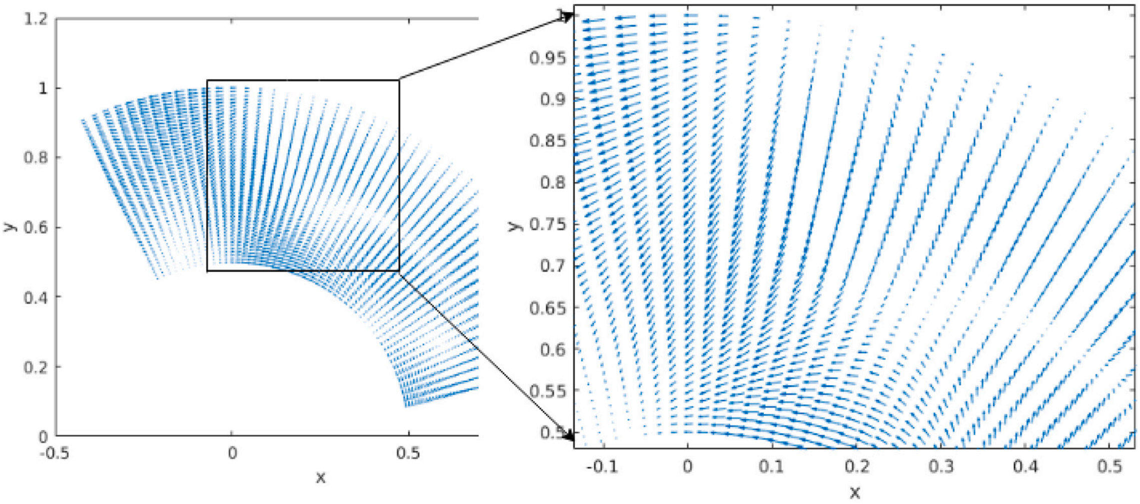

(b) Momentum field of the curvilinear domain at $T = 1.0$

Fig. 10. Plots of the momentum vector field at time $T = 1.0$.

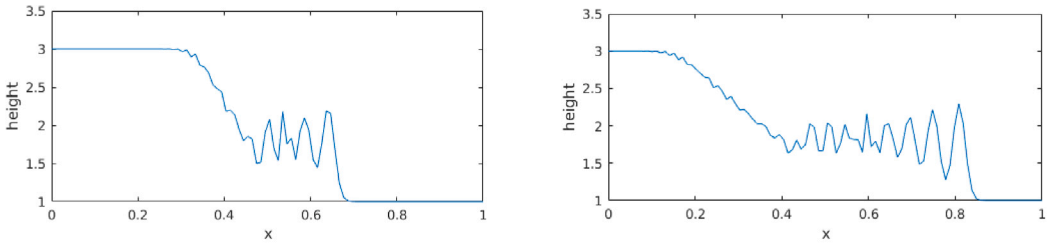

(a) $t = 0.10$ (b) $t = 0.20$

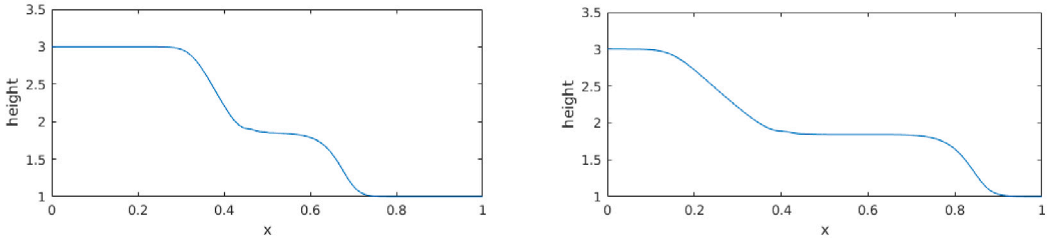

(c) $t = 0.10$ (d) $t = 0.20$

Fig. 11. 1-D Dam break simulation using 4th-order SBP-SAT scheme. Water surface profile after dam failure at time $t = 0.10, 0.20$. (a), (b)-without diffusion and (c), (d)-with diffusion.

We linearize (A.3) by perturbing a smooth solution $(\bar{h}, \bar{u}, \bar{v})$, to $h(\cdot,t) = \bar{h} + \tilde{h}, u(\cdot,t) = \bar{u} + \tilde{u}$ and $v(\cdot,t) = \bar{v} + \tilde{v}$. (These are inserted in (A.3), and by neglecting quadratic terms, we obtain a linear system.) Next, we freeze the coefficients and arrive at the constant-coefficient linear problem

$$U_t + A_0 U_x + B_0 U_y = 0, \tag{A.4}$$

where

$$U = \begin{pmatrix} \tilde{h} \\ \tilde{u} \\ \tilde{v} \end{pmatrix}, \quad A_0 = \begin{pmatrix} u_0 & h_0 & 0 \\ g & u_0 & 0 \\ 0 & 0 & u_0 \end{pmatrix}, \quad B_0 = \begin{pmatrix} v_0 & 0 & h_0 \\ 0 & v_0 & 0 \\ g & 0 & v_0 \end{pmatrix}.$$

Additionally, u_0, v_0 and h_0 represent the constant mean fluid velocities and height, respectively. (See [23,24] for more information on linearizing and localizing equations.)

The system (A.4) is symmetrized by

$$S = \begin{pmatrix} g/c & 0 & 0 \\ 0 & 1 & 0 \\ 0 & 0 & 1 \end{pmatrix},$$

where $c = \sqrt{gh_0}$ is the gravity wave speed. (See [19,27] for further information on symmetrization.) We multiply (A.4) by S to obtain

$$w_t + A w_x + B w_y = 0, \tag{A.5}$$

where $A = SA_0S^{-1}$ as well as $B = SB_0S^{-1}$ are symmetrized matrices given by

$$w = SU = \begin{pmatrix} g\tilde{h}/c \\ \tilde{u} \\ \tilde{v} \end{pmatrix}, \quad A = \begin{pmatrix} u_0 & c & 0 \\ c & u_0 & 0 \\ 0 & 0 & u_0 \end{pmatrix}, \quad B = \begin{pmatrix} v_0 & 0 & c \\ 0 & v_0 & 0 \\ c & 0 & v_0 \end{pmatrix}.$$

Eq. (A.5) is the linearized and symmetrized form of the SWE in a Cartesian domain.

Appendix B. Boundary conditions

B.1. Far-field (open) boundary conditions

Far-field (open) boundary conditions were derived in [19], and we repeat their results for the reader's convenience. To reduce notation, we focus on the boundary at $x = 0$ and ignore the other boundaries,

Table B.9
Different flow conditions based on (B.4) and their sign of eigenvalues. The last column lists the number of boundary conditions in 2-D.

	u_0	$u_0 + c$	$u_0 - c$	2-D
Subcritical (outflow)	−	+	−	1
Subcritical (inflow)	+	+	−	2
Supercritical (outflow)	−	−	−	0
Supercritical (inflow)	+	+	+	3

$$\|w(t,x,y)\|_t^2 = \int_{x=0} w^T A w dy, \tag{B.1}$$

as they can be treated in a similar way.

Since A is symmetric we can diagonalize it as $R_1^T A R_1 = \Lambda_1$, where

$$\Lambda_1 = \begin{pmatrix} u_0 & 0 & 0 \\ 0 & u_0 + c & 0 \\ 0 & 0 & u_0 - c \end{pmatrix} \quad \text{and} \quad R_1 = \begin{pmatrix} 0 & 1/\sqrt{2} & -1/\sqrt{2} \\ 0 & 1/\sqrt{2} & 1/\sqrt{2} \\ 1 & 0 & 0 \end{pmatrix}.$$

Next, A is decomposed as

$$A = R_1 \Lambda_1^+ R_1^T + R_1 \Lambda_1^- R_1^T = A^+ + A^-, \tag{B.2}$$

where, $\Lambda_1^{+,-}$ are diagonal matrices holding the positive and negative eigenvalues, respectively. The continuous energy (B.1) then becomes

$$\|w(t,x,y)\|_t^2 = \int_{x=0} w^T A^+ w dy + \int_{x=0} w^T A^- w dy. \tag{B.3}$$

Boundary conditions must ensure that the growth of $\|w\|_t^2$ is bounded. At $x = 0$, A^- do not contribute to the growth of $\|w\|_t^2$. To bound the A^+-term, we need as many boundary conditions as positive eigenvalues. The sign of the eigenvalues changes with the sign of the normal velocity u_n and the Froude number, which is given as

$$\frac{|u_n|}{c} = \begin{cases} < 1, & \text{Subcritical inflow/outflow} \\ > 1, & \text{Supercritical inflow/outflow.} \end{cases} \tag{B.4}$$

The four possibilities and the necessary (and sufficient) number of boundary conditions are shown in Table B.9.

Following [19], we use the characteristic far-field conditions,

$$A^+ w = A^+ g, \tag{B.5}$$

and recast (B.3) as,

$$\|w(t,x,y)\|_t^2 \quad \leq \quad \int_{x=0} w^T A^+ w dy - 2\int_{x=0} w^T A^+ (w - g) dy = 0, \tag{B.6}$$

or,

$$\|w(t,x,y)\|_t^2 \quad \leq \quad -\int_{x=0}(w-g)^T A^+(w-g)dy + \int_{x=0} g^T A^+ g dy. \qquad \text{(B.7)}$$

The results are then summarized in the following proposition:

Proposition 5. *Let $R_1^T A R_1 = \Lambda_1$ and $R_2^T B R_2 = \Lambda_2$ where $\Lambda_i = diag(\omega_i, \omega_i + c, \omega_i - c)$, $i = 1, 2$, with $\omega_1 = u_0$ and $\omega_2 = v_0$, respectively. Then the far-field boundary conditions*

$$\begin{aligned} A^+ w &= A^+ g_1, \quad x = 0, \qquad & A^- w &= A^- g_2, \quad x = L_1, \\ B^+ w &= B^+ g_3, \quad y = 0, \qquad & B^- w &= B^- g_4, \quad y = L_2, \end{aligned}$$

lead to (strong) well-posedness of (7), where $g_l, l = 1, \ldots, 4$ are bounded boundary data.

B.2. No-penetration wall boundary conditions

In the case of a wall at $x = 0$, the physically relevant boundary condition is the no-penetration boundary condition $u_0 = 0$. (That is, the normal velocity is zero.) Returning to (B.1), we insert $u_0 = 0$ in A, and obtain

$$A = \begin{pmatrix} 0 & c & 0 \\ c & 0 & 0 \\ 0 & 0 & 0 \end{pmatrix}. \qquad \text{(B.8)}$$

The no-penetration condition implies that the perturbation $\tilde u = 0$. Using (B.8) and $\tilde u = 0$ results in $w^T A w = 0$, and (B.1) becomes

$$\|w(t,x,y)\|_t^2 = 0. \qquad \text{(B.9)}$$

We have proven the following proposition:

Proposition 6. *The symmetric constant-coefficient SWE (7) with wall boundary conditions $\tilde u = u_0 = 0$ at $x = \{0, L_1\}$ and $\tilde v = v_0 = 0$ at $y = \{0, L_2\}$ is well-posed.*

Remark 2. The boundary $\delta\Omega$ need not represent only one type of physical boundary. It may represent a mix of open and wall boundary conditions.

Appendix C. Energy stability of the 2D Shallow Water Equations

A semi-discrete approximation of (5) is

$$\mathcal{V}_t + \mathbf{D}_x \bar{\mathcal{F}} + \mathbf{D}_y \bar{\mathcal{G}} = \mathsf{S}(\mathcal{V}, \bar g), \qquad \text{(C.1)}$$

where $\mathsf{S}(\mathcal{V}, \bar g)$ which is introduced later in this section, refers to the Simultaneous Approximation Term (SAT) that enforces the boundary conditions.

Analogous to the continuous case, we linearize, symmetrize and freeze the coefficients to arrive at the semi-discrete counterpart of (7)

$$v_t + \mathbf{D}_x(\mathbf{A}v) + \mathbf{D}_y(\mathbf{B}v) = \mathsf{S}(v, \bar g). \qquad \text{(C.2)}$$

In (C.2), v is the numerical approximation vector of w in (7), $\mathbf{A} = (I_y \otimes I_x \otimes A)$ and $\mathbf{B} = (I_y \otimes I_x \otimes B)$. We now apply the energy analysis to (C.2), and use the SBP properties to arrive at

$$\begin{aligned} &\|v\|_t^2 - v^T \mathbf{P}_y \mathbf{E}_{0x}(\mathbf{A}v) + v^T \mathbf{P}_y \mathbf{E}_{1x}(\mathbf{A}v) - v^T \mathbf{P}_x \mathbf{E}_{0y}(\mathbf{B}v) + v^T \mathbf{P}_x \mathbf{E}_{1y}(\mathbf{B}v) \\ &= 2v^T \mathbf{P}\mathsf{S}(v, \bar g). \end{aligned} \qquad \text{(C.3)}$$

The above expression corresponds to a discrete equivalent of (10). To reduce notation, we focus on the boundary $x = x_0$ and ignore all other boundary terms by assuming that they are stable. Hence, we consider

$$\|v\|_t^2 - v^T \mathbf{P}_y \mathbf{E}_{0x}(\mathbf{A}v) = 2v^T \mathbf{P}\mathsf{S}_{x_0}(v, \bar g), \qquad \text{(C.4)}$$

where S_{x_0} is the x_0-part of S.

C.1. Discrete far-field boundary conditions

To enforce the characteristic far-field conditions (B.5), we propose the following S_{x_0} in (C.4):

$$\mathsf{S}_{x_0}(v, \bar g^f) = -\mathbf{P}_x^{-1}\mathbf{E}_{0x}\mathbf{A}^+(v - \bar g^f). \qquad \text{(C.5)}$$

We introduce $\mathbf{A} = \mathbf{A}^+ + \mathbf{A}^-$ where $\mathbf{A}^{+/-} = (I_y \otimes I_x \otimes A^{+/-})$ and $A^{+/-}$ are given in (B.2), and substitute (C.5) into (C.4) to obtain

$$\|v\|_t^2 - v^T \mathbf{P}_y \mathbf{E}_{0x}(\mathbf{A}^+ + \mathbf{A}^-)v = -2v^T \mathbf{E}_{0x}\mathbf{P}_y \mathbf{A}^+(v - \bar g^f), \qquad \text{(C.6)}$$

In analogy with (B.7), we recast (C.6) to obtain the estimate,

$$\|v\|_t^2 \leq -(v - \bar g^f)^T \mathbf{P}_y \mathbf{E}_{0x}\mathbf{A}^+(v - \bar g^f) + \bar g^{fT}\mathbf{E}_{0x}\mathbf{P}_y \mathbf{A}^+ \bar g^f.$$

The other boundaries can be handled similarly, and we summarize the results in the following proposition:

Proposition 7. *The following penalty (SAT) terms lead to the stability of the scheme (C.2):*

$$\begin{aligned} &-\mathbf{P}_x^{-1}\mathbf{E}_{0x}\mathbf{A}^+(v - \bar g_1^f), \quad x = x_0, \qquad \mathbf{P}_x^{-1}\mathbf{E}_{1x}\mathbf{A}^-(v - \bar g_2^f), \quad x = x_M, \\ &-\mathbf{P}_y^{-1}\mathbf{E}_{0y}\mathbf{B}^+(v - \bar g_3^f), \quad y = y_0, \qquad \mathbf{P}_y^{-1}\mathbf{E}_{1y}\mathbf{B}^-(v - \bar g_4^f), \quad y = y_N, \end{aligned}$$

where $\bar g_l^f, l = 1, \ldots, 4$ is the boundary data defined as in (22).

C.2. Discrete no-penetration wall boundary condition

To enforce the no-penetration condition $u_0 = \tilde u = 0$ discretely at $x = x_0$, we use (C.5) and replace $\bar g^f$ with $\bar g^w = (g\tilde h/c, -\tilde u, \tilde v)$, which is obtained by substituting $\tilde u \to -\tilde u$ into the solution $w = (g\tilde h/c, \tilde u, \tilde v)^T$ at x_0. Note that, $\bar g^w - w = 0$, is equivalent to $\tilde u = 0$ Furthermore, the no-penetration boundary condition implies that $u_0 = 0$ in $\mathbf{A}$.

Now, for the stability of the semi-discrete problem, we require that

$$v^T \mathbf{P}_y \mathbf{E}_{0x}(\mathbf{A}v - 2\mathbf{A}^+(v - \bar g^w)) \leq 0. \qquad \text{(C.7)}$$

In (C.7), $\mathbf{A} = (I_y \otimes I_x \otimes A)$ where A is the symmetric matrix defined in (7). Let $v_{0j} = (v_{0j1}, v_{0j2}, v_{0j3})^T$ be the solution vector at the (x_0, y_j)th point at the boundary. Hence, we have the solution vector v_{0j} as $(g\tilde h_{0j}, \tilde u_{0j}, \tilde v_{0j})^T$. We rewrite (C.7) in component form

$$\sum_j v_{0j}^T P_{yj}(Av_{0j} - 2A^+(v_{0j} - \bar g_{0j}^w)) \leq 0, \qquad \text{(C.8)}$$

where $P_{yj} > 0$ is the jth diagonal element of P_y. Using $u_0 = 0$ in A, we have $A = \begin{pmatrix} 0 & c & 0 \\ c & 0 & 0 \\ 0 & 0 & 0 \end{pmatrix}$ and $A^+ = \begin{pmatrix} c/2 & c/2 & 0 \\ c/2 & c/2 & 0 \\ 0 & 0 & 0 \end{pmatrix}$. Now, taking the jth term of (C.8) (and dropping the indices), we obtain

$$v^T A v - 2v^T A^+(v - \bar g) = 2g\tilde h\tilde u - 2g\tilde h\tilde u - 2c\tilde u^2 \leq 0. \quad \square$$

We summarize the results for all boundaries in the following proposition.

Proposition 8. *The following penalty (SAT) terms lead to the stability of the scheme (C.2):*

$$\begin{aligned} &-\mathbf{P}_x^{-1}\mathbf{E}_{0x}\mathbf{A}^+(v - \bar g_1^w), \quad x = x_0, \qquad \mathbf{P}_x^{-1}\mathbf{E}_{1x}\mathbf{A}^-(v - \bar g_2^w), \quad x = x_M, \\ &-\mathbf{P}_y^{-1}\mathbf{E}_{0y}\mathbf{B}^+(v - \bar g_3^w), \quad y = y_0, \qquad \mathbf{P}_y^{-1}\mathbf{E}_{1y}\mathbf{B}^-(v - \bar g_4^w), \quad y = y_N, \end{aligned}$$

where $\bar g_l^w, l = 1, \ldots, 4$ is boundary data projected at a boundary.

References

[1] Asumadu-Sarkodie S, Owusu PA, Jayaweera HMPC. Flood risk management in Ghana: A case study in Accra. Adv Appl Sci Res 2015;6(4):196–201.

[2] Sakyi A, Amoako-Yirenkyi P, Dontwi IK. A formal homogenization approach to piping flow erosion with deposition in a spatially heterogeneous soil. J Adv Math Comput Sci 2020;35(3):26–45.

[3] Sakyi A, Amoako-Yirenkyi P, Dontwi IK. A rigorous homogenization for a two-scale convergence approach to piping flow erosion with deposition in a spatially heterogeneous soil. J Adv Math Comput Sci 2020.
[4] Tengani C, Aigbavboa CO. Addressing flood challenges in Ghana: A case of the Accra Metropolis. In: International conference on infrastructure development in Africa. 2016, p. 1–8.
[5] Teng J, Jakeman AJ, Vaze J, Croke BFW, Dutta D, Kim S. Flood inundation modelling: A review of methods, recent advances and uncertainty analysis. Environ Model Softw 2017;90:201–16.
[6] Alcrudo F, editor. A state of the art review on mathematical modelling of flood propagation. 2004.
[7] Chow VT. Open channel hydraulics. MacGraw–Hill Book Co. Inc.; 1959.
[8] Cunge JA, Holly FM, Verwey A. Practical aspects of computational river hydraulics. Pitman: London, U.K.; 1980.
[9] Akan AO. Open channel hydraulics. Butterworth-Heinemann; 2006.
[10] Abbott MB. Computational hydraulics. Ashgate Pub. Comp.; 1992.
[11] Kreiss H-O, Oliger J. Comparison of accurate methods for the integration of hyperbolic equations. Tellus 1972;XXIV(3).
[12] Swartz B, Wendroff B. The relative efficiency of finite difference and finite element methods. I: Hyperbolic problems and splines. SIAM J Numer Anal 1974;11(5):979–93.
[13] Gustafsson B, Kreiss HO, Oliger J. Time dependent problems and difference methods. New York: John Wiley & Sons; 2013.
[14] Lundgren L, Mattsson K. An efficient finite difference method for the shallow water equations. J Comput Phys 2020;422:109784.
[15] Poochinapan K, Wongsaijai B, Disyadej T. Efficiency of high-order accurate difference schemes for the Korteweg-de Vries equation. Math Probl Eng 2014;2014:862403.
[16] Chen C, Zhang X, Liu Z. A high-order compact finite difference scheme and precise integration method based on modified Hopf-Cole transformation for numerical simulation of n-dimensional Burgers' system. Appl Math Comput 2020;372:125009.
[17] Ruggiu AA, Nordström J. Multigrid schemes for high order discretizations of hyperbolic problems. J Sci Comput 2020;82:62.
[18] Durran DR. Numerical methods for fluid dynamics with applications to geophysics, Vol. 516 pp. Springer; 2010.
[19] Ghader S, Nordström J. Revisiting well-posed boundary conditions for the shallow water equations. Dyn Atmos Oceans 2014;66:1–9.
[20] Nordström J, Winters AR. A linear and nonlinear analysis of the shallow water equations and its impact on boundary conditions. J Comput Phys 2022;111254:463.
[21] Roache PJ. Code verification by the method of manufactured solutions. Trans ASME, J Fluids Eng 2002;124:4–10.
[22] Salari K, Knupp P. Code verification by the method of manufactured solutions. Tech. Rep., Sandia Report, Sandia National Laboratories; 2000.
[23] Gustafsson B. High order difference methods for time dependent PDE. Berlin, Heidelberg: Springer-Verlag; 2008.
[24] Kreiss H-O, Lorenz J. Initial boundary value problems and the Navier-Stokes equations. New York: Academic Press; 1989.
[25] Svärd M, Carpenter MH. A stable high-order finite difference scheme for the compressible Navier-Stokes equations, no-slip wall boundary conditions. J Comput Phys 2008;227(10):4805–24.
[26] Svärd M, Carpenter MH, Nordström J. A stable high-order finite difference scheme for the compressible Navier-Stokes equations, far-field boundary conditions. J Comput Phys 2007;225(1):1020–38.
[27] Nordström J, Svärd M. Well-posed boundary conditions for the Navier-Stokes equations. SIAM J Numer Anal 2005;43:1231–55.
[28] Strikwerda JC. Initial boundary value problems for incompletely parabolic systems. Comm Pure Appl Math 1977;30:797–822.
[29] Kreiss H-O, Scherer G. Finite element and finite difference methods for hyperbolic partial differential equations. Mathematical aspects of finite elements in partial differential equations. Academic Press, Inc.; 1974.
[30] Gustafsson B. The convergence rate for difference approximations to general mixed initial boundary value problems. SIAM J Numer Anal 1981;18(2):179–90.
[31] Gustafsson B. The convergence rate for difference approximations to mixed initial boundary value problems. Math Comp 1975;29(130):396–406.
[32] Svärd M, Nordström J. On the convergence rates of energy-stable finite-difference schemes. J Comput Phys 2019;397:108819.
[33] Svärd M, Nordström J. Review of summation-by-parts schemes for initial-boundary-value problems. J Comput Phys 2014;268:17–38.
[34] Fernandez DC, Hicken JE, Zingg DW. Review of summation-by-parts operators with simultaneous approximation terms for the numerical solution of partial differential equations. Comput & Fluids 2014;95:171–96.
[35] Horn RA, Johnson CR. Matrix analysis. 2nd ed.. Cambridge University Press; 2012.
[36] Loan CFV. The ubiquitous Kronecker product. J Comput Appl Math 2000;123:85–100.
[37] Svärd M, Nordström J. On the order of accuracy for difference approximations of initial-boundary value problems. J Comput Phys 2006;218(1):333–52.
[38] Nordström J. Error bounded schemes for time-dependent hyperbolic problems. SIAM J Sci Comput 2007;30:46–59.